Geochemistry, Geophysics, Geosystems

Supporting Information for

Correction of interstitial water changes in calibration methods applied to XRF core-scanning major elements in long sediment cores: case study from the South China Sea

Quan Chen[1,2,*], Catherine Kissel[2], Aline Govin[2], Zhifei Liu[1], Xin Xie[1]

1. State Key Laboratory of Marine Geology, Tongji University, Shanghai, 200092, China

2. Laboratoire des Sciences du Climat et de l'Environnement/IPSL, CEA-CNRS-UVSQ, Université Paris-Saclay, 91198 Gif-sur-Yvette Cedex, France

* Corresponding Author: quan.chen@hotmail.com

Contents of this file

Additional Supporting Information (Files uploaded separately)

Introduction

The reliability of WD-XRF concentrations used as reference datasets for XRF scanning calibration is evaluated in text S1. The detailed descriptions of existing and improved calibrations are introduced in text S2 and S3, respectively. The data used in the XRF scanning calibrations and in the evaluation of calibration methods are included in the supplemental data set S1 and S2. Data set S3 presents the ICP-AES analyses that are used to verify the accuracy of WD-XRF measurements.

Text S1. Accuracy evaluation of WD-XRF element concentrations

The WD-XRF analysis of major elements has been reported to be of high accuracy by various studies [*e.g.* Tsuchiya et al., 1989; Rousseau et al., 1996; Rahmani et al., 2004; Gazulla et al., 2013; Hunt et al., 2014]. Therefore, quantitative element concentrations obtained by energy-dispersive or wavelength-dispersive XRF have been used as reference datasets for correcting or calibrating XRF-scan intensities in several previous studies [*e.g.* Tjallingii et al., 2007; Weltje and Tjallingii, 2008; Hennekam and De Lange, 2012]. To further confirm the reliability of WD-XRF concentrations used as reference datasets in this study, inductive coupled plasma atomic emission spectrometer (ICP-AES) analyses were performed on 22 discrete samples. Dried and ground bulk sediments were heated at 600°C for 4 hours to remove organic matter. Their weights were measured before and after heating to calculate the loss on ignition (LOI). The sediments, together with a series of Chinese rock and sediment standards (*i.e.* GSR5, GSR6 and GSD9), were digested in HF+HNO_3 mixed acid. Major elements were then measured on an IRIS Advantage ICP-AES. The mean relative accuracy estimated from the Chinese rock and sediment standard samples is better than 4%.

WD-XRF concentrations of six major-element oxides are plotted together with ICP-AES data in Fig S1. The associated uncertainties account for the instrument analysis. Because concentrations in bulk sediments are considered, the 1% analytical uncertainty of LOI [Heiri et al. 2001] is also taken into account in ICP-AES uncertainties.

WD-XRF and ICP-AES concentrations are very consistent within the analytical uncertainties and they follow the same variation patterns [Fig. S1a-S1e]. We observe that the ICP-AES concentrations are slightly shifted with respect to the WD-XRF concentrations for all five elements. This may be due to the fact that Si is not measured by the ICP method but deduced from the measurement of all other elements and LOI. The observed shifts may therefore result from erroneous Si evaluation. In addition, the log-ratio values and variations are identical in the two datasets [Fig. S1i-S1v], indicating that the relative proportions of elements are exactly the same, no matter the method (ICP-AES or WD-XRF) used to measure the element concentrations. Because the WD-XRF analytical method allows direct measurements of Si concentrations (which account for about 50% of the geochemical composition of bulk sediments in this study), we prefer to use here WD-XRF measurements as reference datasets for the calibration of geochemical concentrations in core MD12-3432.

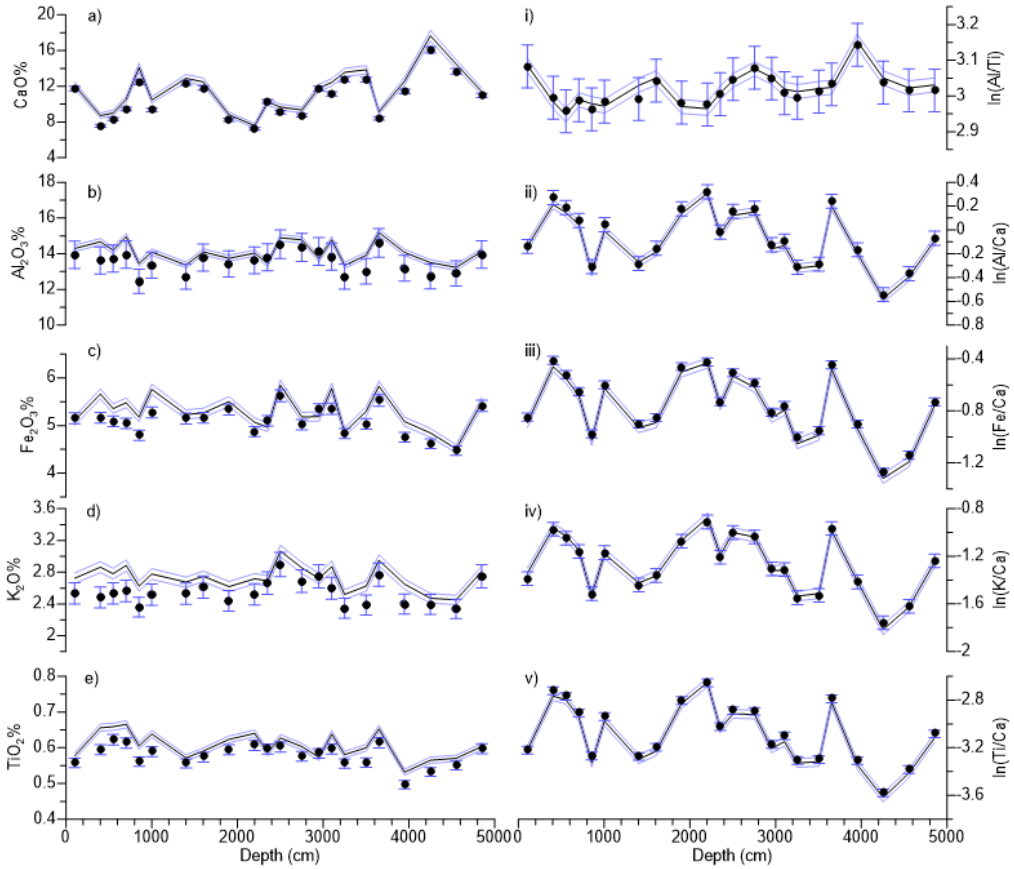

Figure S1. Comparison of ICP-AES and WD-XRF results in terms of oxide concentrations of a) CaO, b) Al_2O_3, c) Fe_2O_3, d) K_2O, and e) TiO_2, and of log-ratios i) ln(Al/Ti), ii) ln(Al/Ca), iii) ln(Fe/Ti), iv) ln(K/Ca), and v) ln(Ti/Ca). ICP-AES results (black lines) are plotted with their analytical uncertainties (blue lines), and WD-XRF results (black dots) are plotted with analytical uncertainties (blue error bar).

Text S2. Description of existing XRF calibration methods

S2.1 Correction for water absorption effect

Based on high-resolution analysis of three short sediment sequences, Hennekam and De Lange [2012] proposed a routine approach to correct the influence of water absorption on log-ratios of XRF-scan intensities due to variations in water film thickness. According to the Lambert-Beer law [Hubbell, 1982] that describes the relationship between original intensity and residual intensity of a specific X-ray before and after passing through a homogeneous medium, the original intensity $I_{e,d}'$ of element *e* at depth *d* can be obtained following equation S1 by assuming that Cl intensity changes only represent variations in water film thickness:

$$I_{e,d}' = I_{e,d} \exp(\mu_{e,Cl} I_{Cl,d}) \quad \text{(eq S1)}$$

where $I_{e,d}$ is the intensity obtained for element *e* at depth *d* by XRF scanning, $\mu_{e,Cl}$ is the specific attenuation coefficient for element *e*, and $I_{Cl,d}$ is the XRF scanning Cl intensity at depth *d*. $\mu_{e,Cl}$ is empirically obtained by changing its value to reach an optimal linear correlation between corrected XRF-scan intensities and WD-XRF concentrations of the target element.

In the case of core MD12-3432, the entire WD-XRF dataset (102 samples) was used to determine the $\mu_{e,Cl}$ value for each element. The NMS and MLC methods (named as W_NMS and W_MLC) were then performed on the water-corrected intensities.

S2.2 Normalized median-scaled calibration (NMS)

In the NMS method [Lyle et al., 2012; Lyle and Backman 2013], XRF-scan intensities are first scaled to the range of sedimentary component concentration values, independently for each element. Indeed, various elements do not have the same efficiency of producing characteristic X-ray, and normalizing on XRF-scan intensities would, therefore, produce awry relative proportions with respect to the element compositions. The median-scaled value of an element component *e* at depth *d* ($S_{e,d}$) is:

$$S_{e,d} = W_{e,M} \times I_{e,d} / I_{e,M} \quad \text{(eq S2)}$$

where $W_{e,M}$ is the median concentration of the corresponding sedimentary component *e* from the WD-XRF calibration dataset, $I_{e,d}$ is the XRF-scan intensity of element component *e* at depth *d*, and $I_{e,M}$ is the median intensity value of element component *e* over the entire XRF-scan dataset.

In a second step, the median-scaled values are summed and normalized to 100% to eliminate the variability caused by differences in density and cracks. The normalized median-scaled value of element component e at depth d ($NMS_{e,d}$) is calculated as:

$$NMS_{e,d} = S_{e,d} \times 100\% / \sum S_d \quad \text{(eq S3)}$$

where $S_{e,d}$ represents the median-scaled value of element component *e* at depth *d*, and $\sum S_d$ is the sum of median-scaled values of the six sedimentary components at depth *d*.

Finally, normalized median-scaled values are calibrated against WD-XRF concentrations of sedimentary components through linear regression equations, providing high-resolution calibrated concentrations of each sedimentary component in bulk sediments.

S2.3 Multivariate log-ratio calibration (MLC)

MLC [Weltje et al., 2015] is developed from the previously proposed log-ratio calibration equation (LRCE) approach [Weltje and Tjallingii, 2008]. The use of centered log-ratios (clr) and partial least squares regression allows the MLC method to take account of multiple covariances at the same time [Weltje et al., 2015]. Therefore the MLC method can directly fit the absorption and enhancement of intensities caused by the presence of unmeasured elements. Benefiting from the multivariate calibration, MLC can also predict bulk element concentrations by including the union of unmeasured elements as one "element" [Weltje et al., 2015]. Moreover, the

improved workflow, which includes uncertainty estimation and automatic selection of calibration samples, enhances the predictive power of the MLC method [Weltje et al., 2015].

To perform the MLC, XRF-scan element intensities and WD-XRF element concentrations are first transformed to centered log-ratios, and then scaled with the inverse of their uncertainties determined from replicate measurements. The calibration dataset can be automatically determined using a hierarchical cluster analysis of the scaled clr-transformed intensities. A reasonable model of calibration is then carried out using the calibration dataset by means of partial least squares regression, and is applied to the entire XRF-scan dataset for calibration. The calibration approach has been implemented in the XELERATE software available on line [www.ascar.nl].

S2.4 Comparison between NMS and W-NMS results and between MLC and W-MLC results

The water absorption correction (described in text S2.1) improves the accuracy of NMS- and MLC-calibrated results by reducing their MSRE [Table S1]. Moreover, as indicated by the increased average R^2 [Table S1], applying the water absorption correction improves their correlation to WD-XRF concentrations. Therefore, W_NMS and W_MLC are discussed in the main text (section 5).

However, calibrated W_NMS and W_MLC results remain quite similar to the original NMS and MLC calibrated results, respectively, and deviations from WD-XRF concentrations data are still observed for all methods in the top sections of core MD12-3234 [Fig. S2]. This comparison confirms our conclusions (section 5.3 of the main text) that the water absorption correction is insufficient to correct downcore water changes in our case study.

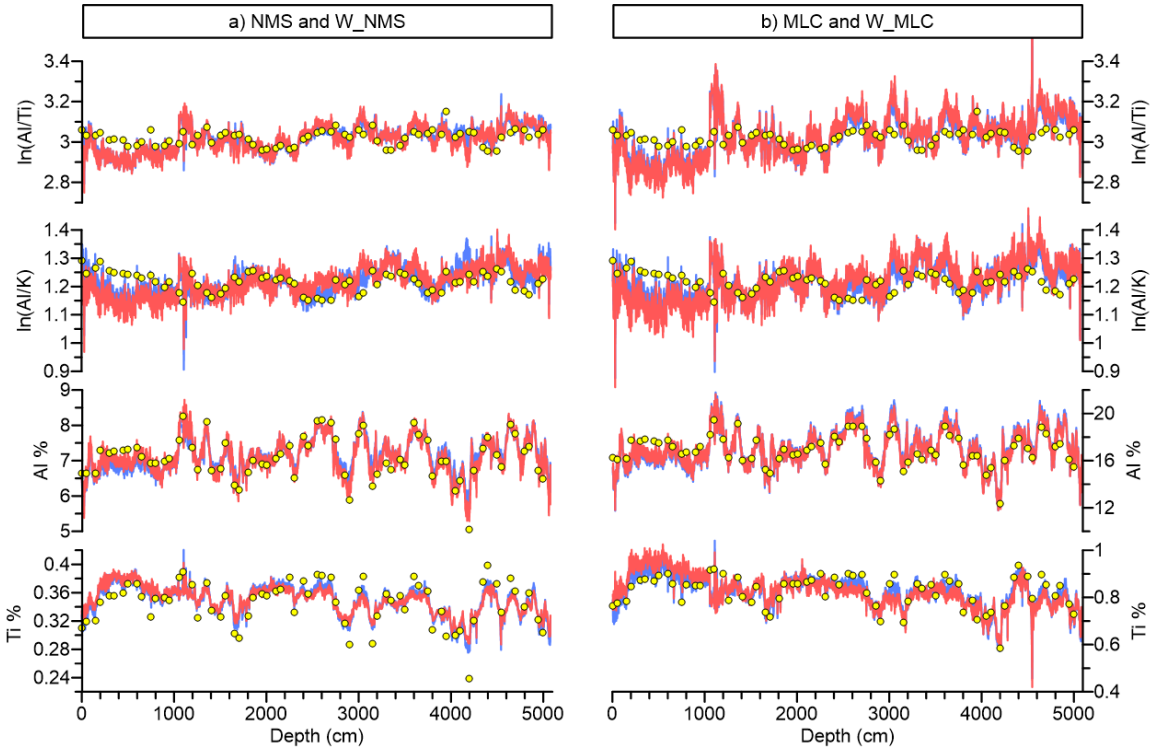

Figure S2. Calibration results. NMS (red lines) and W_NMS (blue lines) results are shown in the left panel (a), MLC (red lines) and W_MLC (blue lines) results are presented in the right panel (b). WD-XRF evaluation data are shown as yellow dots. Note that Al% and Ti% calibrated by MLC and W_MLC refer to relative proportions of Al and Ti.

Text S3. Description of proposed improved calibration methods

S3.1 Normalized polynomial-scaled calibration (NPS)

In the NPS approach, the polynomial-scaled value of element component *e* at depth *d* is first calculated by the equation S4:

$$PS_{e,d} = (a' \times d^2 + b' \times d + c') \times I_{e,d} / (a \times d^2 + b \times d + c) \quad \text{(eq S4)}$$

where $I_{e,d}$ is the XRF-scan intensity of element component *e* at depth *d*; a, b, c and a′, b′, c′ are the coefficients of quadratic polynomials fitted through the XRF-scan intensities and WD-XRF concentrations of element component *e*, respectively [Table S2].

In the second step, this polynomial-scaled value is normalized to the sum of WD-XRF concentrations for all element components, instead of to unity as in the NMS, because the sum of all component concentrations is diluted by components that are not included in the calibration (*e.g.* organic matter, Na and Mg) and varies below 90% along the core. As the calibration dataset is smaller than polynomial-scaled dataset, WD-XRF concentration sums are interpolated to fit the polynomial-scaled dataset. The normalized polynomial-scaled value of element component *e* at depth *d* is then determined using the following equation:

$$NPS_{e,d} = \sum W_d \times PS_{e,d} / \sum S_d \quad \text{(eq S5)}$$

where $\sum W_d$ is the interpolated sum of WD-XRF concentrations for all element components at depth *d*, $PS_{e,d}$ is obtained by equation S4, and $\sum S_d$ is the sum of polynomial-scaled values of all element components at depth *d*.

Finally, normalized polynomial-scaled data are calibrated against WD-XRF concentrations for the six chosen major element components using linear regression equations.

S3.2 Polynomial corrected multivariate log-ratio calibration (P_MLC)

In the polynomial-corrected MLC (P_MLC) approach, XRF-scan element intensities are first summed to unity. A polynomial correction is then performed in log-ratio space on all possible ratio combinations. The polynomial-corrected log-ratio of element e and D at depth d ($P_{eD,d}$) is calculated using equation S6:

$$P_{eD,d} = (a' \times d^2 + b' \times d + c') + \ln(I_{e,d} / I_{D,d}) - (a \times d^2 + b \times d + c) \quad \text{(eq S6)}$$

where $I_{e,d}$ and $I_{D,d}$ are normalized XRF-scan intensities of element *e* and *D* at depth *d*; a, b, c and a′, b′, c′ are the coefficients of quadratic polynomial fitted through the XRF-scan intensities and WD-XRF element concentrations, respectively [Table S2].

All polynomial-corrected log-ratios are then tested to select the element used as common denominator in log-ratios in order to obtain the most robust correction. In this case of core MD12-3432, Ca is chosen as the common denominator. An inverse additive log-ratio transformation is then performed on the polynomial-corrected log-ratios with Ca as common denominator, transforming them to relative proportions of intensities. The transformed dataset is further calibrated using the MLC approach.

References

Gazulla, M. F., M. Orduña, S. Vicente, and M. Rodrigo (2013), Development of a WD-XRF analysis method of minor and trace elements in liquid petroleum products, Fuel, 108, 247-253. doi: 10.1016/j.fuel.2013.02.049

Heiri, O., A. Lotter, and G. Lemcke (2001), Loss on ignition as a method for estimating organic and carbonate content in sediments: reproducibility and comparability of results, Journal of Paleolimnology, 25(1), 101-110. doi: 10.1023/A:1008119611481

Hennekam, R., and G. de Lange (2012), X-ray fluorescence core scanning of wet marine sediments: methods to improve quality and reproducibility of high-resolution paleoenvironmental records, Limnology and Oceanography: Methods, 10(12), 991-1003. doi: 10.4319/lom.2012.10.991

Hubbell, J. H. (1982), Photon mass attenuation and energy-absorption coefficients, The International Journal of Applied Radiation and Isotopes, 33(11), 1269-1290. doi: 10.1016/0020-708X(82)90248-4

Hunt, A., D. Dvoracek, M. Glascock, and R. Speakman (2014), Major, minor and trace element mass fractions determined using ED-XRF, WD-XRF and INAA for five certified clay reference materials: NCS DC 60102-60105; NCS DC 61101 (GBW 03101A, 03102A, 03103, and 03115), Journal of Radioanalytical & Nuclear Chemistry, 302(1), 505-512. doi: 10.1007/s10967-014-3266-z

Lyle, M., A. O. Lyle, T. Gorgas, A. Holbourn, T. Westerhold, E. Hathorne, K. Kimoto, and S. Yamamoto (2012), Data report: raw and normalized elemental data along the Site U1338 splice from X-ray fluorescence scanning. In Pälike, H., M. Lyle, H. Nishi, I. Raffi, K. Gamage, A. Klaus, and the Expedition 320/321 Scientists, Proc. IODP, 320/321: Tokyo (Integrated Ocean Drilling Program Management International, Inc.). doi:10.2204/iodp.proc.320321.203.2012

Lyle, M., and J. Backman (2013), Data report: calibration of XRF-estimated $CaCO_3$ along the Site U1338 splice, In Pälike, H., M. Lyle, H. Nishi, I. Raffi, K. Gamage, A. Klaus, and the Expedition 320/321 Scientists, Proc. IODP, 320/321: Tokyo (Integrated Ocean Drilling Program Management International, Inc.). doi:10.2204/iodp.proc.320321.205.2013

Rahmani, A., F. Benyaïch, M. Bounakhla, E. Bilal, J. Moutte, J. J. Gruffat, and F. Zahry (2004), Étude comparative des techniques d'analyse par fluorescence X à dispersion d'énergie (ED-XRF) et à dispersion de longueur d'onde (WD-XRF), et par spectrométrie d'émission atomique à source plasma couplée par induction (ICP-AES), Journal De Physique IV, 118, 447-455. doi : 10.1051/jp4:2004118052

Rousseau, R. M., J. P. Willis, and A. R. Duncan (1996), Practical XRF Calibration Procedures for Major and Trace Elements, X-Ray Spectrometry, 25(4), 179-189. doi: 10.1002/(SICI)1097-4539(199607)25:4<179::AID-XRS162>3.0.CO;2-Y

Tjallingii, R., U. Röhl, M. Kölling, and T. Bickert (2007), Influence of the water content on X-ray fluorescence core-scanning measurements in soft marine sediments, Geochemistry, Geophysics, Geosystems, 8(2). doi: 10.1029/2006GC001393

Tsuchiya, N., T. Shibata, Y. Koide, M. Owada, E. Takazawa, Y. Goto, J. H. Choi, S. Terada, and Y. Hariya (1989), Major Element Analysis of Rock Samples by X-ray Fluorescence Spectrometry, using Scandium Anode Tube, Journal of the Faculty of Science, Hokkaido Unviversity, XXII(3), 489-502. http://hdl.handle.net/2115/36761

Weltje, G. J., and R. Tjallingii (2008), Calibration of XRF core scanners for quantitative geochemical logging of sediment cores: Theory and application, Earth and Planetary Science Letters, 274(3–4), 423-438. doi: 10.1016/j.epsl.2008.07.054

Weltje, G. J., M. Bloemsma, R. Tjallingii, D. Heslop, and I. W. Croudace (2015), Prediction of Geochemical Composition from XRF Core Scanner Data: A New Multivariate Approach Including Automatic Selection of Calibration Samples and Quantification of Uncertainties, in Micro - XRF Scanning of Sediment Cores, edited by R. G. Rothwell and I. W. Croudace, Springer.

	MSRE	R^2						
		Al	Si	K	Ca	Ti	Fe	Average
NMS	0.00250	0.92	0.96	0.78	0.98	0.68	0.45	0.80
MLC	0.00289	0.85	0.96	0.78	0.98	0.46	0.20	0.71
W_NMS	0.00169	0.93	0.94	0. 92	0.98	0.84	0.66	0.88
W_MLC	0.00183	0.81	0.96	0.91	0.99	0.68	0.49	0.81

Table S1. Comparative performance of the NMS, W_NMS, MLC and W_MLC calibrations based on the independent WD-XRF evaluation dataset.

	XRF core-scanning			WD-XRF		
	a	*b*	*c*	*a′*	*b′*	*c′*
NPS						
Al_2O_3	-1.80469×10^{-4}	1.68432×10^{0}	8.97978×10^{3}	2.78273×10^{-9}	-8.40326×10^{-5}	1.37066×10^{1}
SiO_2	-2.45332×10^{-3}	1.79966×10^{1}	1.00061×10^{5}	-1.81234×10^{-7}	2.41132×10^{-4}	4.51526×10^{1}
K_2O	-1.41146×10^{-3}	1.02346×10^{1}	7.65880×10^{4}	-1.51777×10^{-8}	7.41048×10^{-5}	2.50604×10^{0}
$CaCO_3$	7.41644×10^{-3}	1.63646×10^{1}	3.49452×10^{5}	7.16093×10^{-8}	1.12871×10^{-3}	1.62933×10^{1}
TiO_2	-3.86774×10^{-4}	2.12999×10^{0}	2.59334×10^{4}	-1.23080×10^{-9}	1.69629×10^{-6}	3.50704×10^{-1}
Fe_2O_3	-2.86182×10^{-3}	1.37946×10^{1}	2.67617×10^{5}	9.82231×10^{-9}	-4.98498×10^{-5}	5.19958×10^{0}
P_MLC						
Ln(Al/Ca)	-3.02644×10^{-8}	1.05644×10^{-4}	-3.62151×10^{0}	-1.09977×10^{-9}	-7.01019×10^{-5}	1.22727×10^{-1}
Ln(Si/Ca)	-3.34144×10^{-8}	9.94519×10^{-5}	-1.20827×10^{0}	-5.30853×10^{-9}	-5.91265×10^{-5}	1.18852×10^{0}
Ln(K/Ca)	-2.84439×10^{-8}	6.29718×10^{-5}	-1.47834×10^{0}	-7.18546×10^{-9}	-3.55063×10^{-5}	-1.12705×10^{0}
Ln(Ti/Ca)	-2.62373×10^{-8}	2.14666×10^{-5}	-2.56272×10^{0}	-3.60930×10^{-9}	-6.01153×10^{-5}	-2.90324×10^{0}
Ln(Fe/Ca)	-2.23219×10^{-8}	-7.08975×10^{-6}	-2.29677×10^{-1}	-4.20260×10^{-10}	-7.35452×10^{-5}	-5.66757×10^{-1}

Table S2. Parameters of quadratic polynomial equations applied to XRF-scan element intensities and WD-XRF component concentrations in NPS calibration (equations S4), as well as XRF-scan and WD-XRF element log-ratios in P_MLC calibration (equation S6).

Data Set S1. Discrete measurements of core MD12-3432. WD-XRF data (both calibration and evaluation dataset), dry bulk density and water content are included.

Data Set S2. XRF core scanning data of core MD12-3432 used in the calibration.

Data Set S3. ICP-AES data of core MD12-3432 used to verify the accuracy of WD-XRF analyses.